AIAA JOURNAL
Vol. 45, No. 8, August 2007

# Tip Vortex Conservation on a Helicopter Main Rotor Using Vortex-Adapted Chimera Grids

Markus Dietz,* Manuel Keßler,† Ewald Krämer,‡ and Siegfried Wagner§
*University of Stuttgart, 70569 Stuttgart, Germany*

DOI: 10.2514/1.28643

**This paper presents a method to improve the tip vortex conservation in a computational fluid dynamics simulation of a helicopter main rotor. Our approach uses vortex-adapted Chimera child grids to achieve a local refinement of the grid in the vicinity of the vortex and thus reduce the numerical dissipation of the vortex. The method is applied to the higher-harmonic-control aeroacoustic rotor test case to evaluate its potential with respect to the prediction of blade–vortex interaction airloads. To allow a meaningful comparison with the experimental data, the rotor is trimmed for thrust, as well as for longitudinal and lateral mast moments, using weak fluid–structure coupling with a flight mechanics code. We obtained a good overall agreement with the experimental data for both aerodynamics and blade dynamics. The effect of the improvement in tip vortex conservation is demonstrated by comparison with simulations without Chimera refinement and with the experimental results. It turned out that a very fine grid resolution in the vicinity of the vortex is necessary to capture the blade–vortex interaction airloads. The required grid resolution was provided by a refinement of the vortex-adapted grids, allowing for a very good reproduction of the blade–vortex interaction airloads, especially on the retreating blade side.**

## Nomenclature

| | | |
|---|---|---|
| $C_mMa^2$ | = | sectional pitching moment coefficient |
| $C_nMa^2$ | = | sectional normal force coefficient |
| $F_z$ | = | rotor thrust, N |
| $Ma_{\text{tip}}$ | = | hover tip Mach number |
| $M_x$ | = | rotor mast rolling moment, Nm |
| $M_y$ | = | rotor mast pitching moment, Nm |
| $\alpha_q$ | = | rotor shaft angle, deg |
| $\theta_c$ | = | longitudinal cyclic pitch angle, deg |
| $\theta_s$ | = | lateral cyclic pitch angle, deg |
| $\theta_0$ | = | collective pitch angle, deg |
| $\theta_{3/\text{rev}}$ | = | three-per-revolution higher-harmonic-control amplitude, deg |
| $\mu$ | = | advance ratio |
| $\psi$ | = | rotor azimuth angle, deg |
| $\psi_w$ | = | wake age, deg |
| $\psi_{3/\text{rev}}$ | = | three-per-revolution pitch control phase, deg |

## I. Introduction

THE blade-tip vortices of a helicopter main rotor not only remarkably influence the aerodynamics of the rotor but also have a severe impact on the aeroelastic and acoustic behavior of the rotor. In hover, for instance, at least eight revolutions of the tip vortex have to be included in a numerical simulation to correctly compute the influence of the vortex-induced velocities on the blades and thus to predict the aerodynamics of the rotor correctly [1]. For a slow-descent flight with a low advance ratio, the correct reproduction and conservation of the tip vortices is mandatory to correctly capture blade–vortex interaction (BVI) effects and thus to provide an accurate database for acoustic postprocessing [2]. The effort that is necessary to correctly reproduce the vortex system differs for the different computational methods that can be applied for the analysis. In the case of a vortex-lattice method [3,4], for instance, the vortex system is directly obtained from the interaction of the vortex filaments that are shed from the blade. Thus, no vortex dissipation at all is present and BVI effects can be reproduced with a comparatively low computational effort. The accurate reproduction of the vortex system and the correct prediction of BVI airloads by a computational fluid dynamics (CFD) computation is a more complex task [1]. In the case of a CFD computation, the vortex system results directly from the numerical solution of the Euler or Reynolds-averaged Navier–Stokes (RANS) equations. A separate wake model is thus not needed [5–8]. But this means that the vortices are subject to the numerically caused dissipation of the computational scheme. To minimize the truncation error of the scheme and thus the dissipation of the tip vortices, higher-order schemes and/or very fine grids would be necessary.

In the context of helicopter applications, higher-order spatial schemes are not yet commonly used. The incorporation of higher-order schemes has lagged significantly due to their higher complexity and their lower robustness. However, approved and robust second-order codes for helicopter applications are currently available. Using such a second-order method, one possibility to avoid the usage of very fine grids is the Chimera technique of overlapping grids, in which individual grids (e.g., connected to each blade) are embedded in a background grid [9,10]. To account for the relative motion of the blades and the strong interference effects between aerodynamics and rotor dynamics, the Chimera technique is often applied anyway for the simulation of helicopter rotors [11–15].

Using the Chimera technique, the conservation of the tip vortex shed from a given blade and thus the prediction of its influence on the following blades could be improved by providing a finer background grid. But, dependent on the flight case, this approach can become inefficient, because a large domain must be covered with a fine grid, although the fine grid resolution is only needed in the region of the blade-tip vortex and is unnecessary elsewhere. Our approach circumvents this drawback by adding special vortex-adapted Chimera subgrids. The position of these vortex-adapted grids varies with time to fit the current position of the blade-tip vortex and to cover a predefined wake age. In the present paper, we apply this

Presented as Paper 3478 at the 24th AIAA Applied Aerodynamics Conference, San Francisco, CA, 5–8 June 2006; received 31 October 2006; revision received 28 February 2007; accepted for publication 7 April 2007. 

*Research Assistant, Institute of Aerodynamics and Gasdynamics, Pfaffenwaldring 21.
†Researcher, Institute of Aerodynamics and Gasdynamics, Pfaffenwaldring 21.
‡Head of Institute, Institute of Aerodynamics and Gasdynamics, Pfaffenwaldring 21.
§Former Head of Institute, Institute of Aerodynamics and Gasdynamics, Pfaffenwaldring 21.

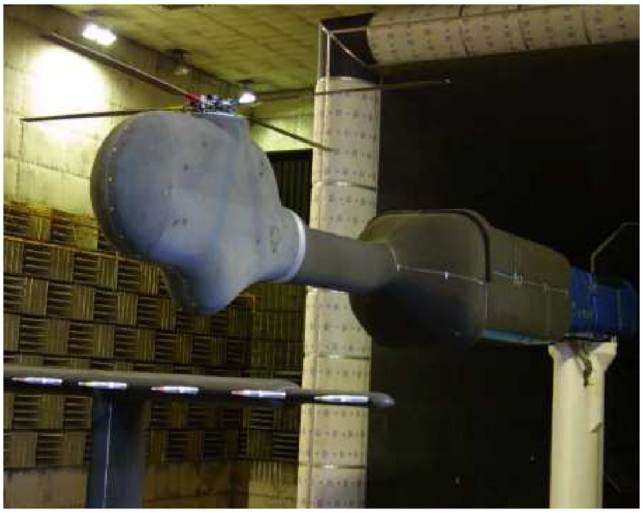

**Fig. 1 HART-2 hingeless rotor model in the DNW wind tunnel.**

technique to a BVI descent flight case to evaluate the benefits of the technique with respect to the prediction of BVI airloads.

For this purpose, the higher-harmonic-control aeroacoustic rotor (HART-2) test case was chosen. In this experimental program, a 40% dynamically scaled model of the Bo105 hingeless main rotor was investigated in the open-jet test section of the German–Dutch Wind Tunnels (DNW) in a slow-descent flight condition. The experimental test setup is given in Fig. 1. Both for the standard [baseline (BL)] case and for two cases featuring an additional three-per-revolution higher-harmonic-control (HHC) input, extensive experimental data for blade dynamics, lift, wake geometry, and noise are available. Therefore, this test case is perfectly suited for the present purpose. Further information on the HART rotor test campaign can be found in [16–18].

To allow a meaningful comparison with the experimental data, an aeroelastic analysis is performed. We use the weak coupling technique [19–22] between the CFD solver FLOWer (DLR, German Aerospace Research Center) and the flight mechanics/computational structural dynamics (CSD) code HOST (Eurocopter). The rotor is trimmed for thrust, as well as longitudinal and lateral mast moments, in all computations by adaption of the collective and the cyclic pitch angles. For the present paper, we will restrict ourselves to the baseline case and the first HHC case, the minimum-noise (MN) case.

## II. Numerical Methods

### A. Computational Structural Dynamics Model

The Eurocopter flight mechanics tool HOST [23] represents a computational environment for simulation and stability analysis of the complete helicopter system. It enables the study of single helicopter components such as isolated rotors, as well as complete configurations with related substructures. As a general-purpose flight mechanics tool, HOST is capable of trimming the rotor based on a lifting-line method with 2-D airfoil tables. The elastic blade model in HOST considers the blade as a quasi-one-dimensional Euler–Bernoulli beam. It allows for deflections in flap and lag direction and elastic torsion along the blade axis. In addition to the assumption of a linear material law, tension elongation and shear deformation are neglected. However, possible offsets between the local cross-sectional center of gravity, tension center, and shear center are accounted for, thus coupling bending and torsional degrees of freedom (DOF). The blade model is based on a geometrically nonlinear formulation, connecting rigid segments through virtual joints. At each joint, elastic rotations are permitted about the lag, flap, and torsion axes. Because the use of these rotations as degrees of freedom would yield a rather large system of equations, the number of equations is reduced by a modal Rayleigh–Ritz approach. A limited set of modelike deformation shapes, together with their weighting factors, are used to yield a deformation description. Therefore, any degree of freedom can be expressed as

$$h(r,\psi) = \sum_{i=1}^{n} q_i(\psi) \cdot \hat{h}_i(r) \tag{1}$$

where $n$ is the number of modes, $q_i$ is the generalized coordinate of mode $i$ (a function of the azimuth angle $\psi$), and $\hat{h}_i$ is the modal shape (a function of the radial position $r$). HOST can be used in conjunction with a prescribed or a free-wake model. For the present investigation, this option was not applied. The choice of the HOST aerodynamic model does not influence the trimmed CFD/CSD solution, because the initial HOST aerodynamic model is completely replaced by the CFD aerodynamics during the coupling process.

### B. Computational Fluid Dynamics Model

In the present study, the DLR FLOWer code [24] was used for the aerodynamics. FLOWer solves the three-dimensional unsteady Euler or Reynolds-averaged Navier–Stokes equations (RANS) in integral form. The equations are derived for a moving frame of reference. Turbulence can be modeled either by algebraic or by transport equation models.

The numerical procedure is based on structured meshes. The spatial discretization uses a finite volume formulation. Both central schemes and several upwind schemes are available for the flux computation. In the case of the central scheme, dissipative terms are explicitly added to damp high-frequency oscillations and to allow sufficiently sharp resolutions of shock waves in the flowfield. On smooth meshes, the scheme is formally of second order in space. The time integration is carried out by an explicit Runge–Kutta scheme featuring convergence acceleration by local time stepping and implicit residual smoothing. The solution procedure is embedded into a sophisticated multigrid algorithm, which allows standard single-grid computations and successive grid refinement. Unsteady calculations are carried out using the implicit dual-time-stepping scheme, which reduces the solution of a physical time step to a steady-state solution in pseudotime. This approach is very effective because all convergence acceleration methods mentioned earlier can be used.

The code is written in a flexible block-structured form, enabling treatment of complex aerodynamic configurations with any mesh topology. FLOWer is capable of calculating flows on moving grids (arbitrary translatory and rotatory motion). For this purpose, the RANS equations are transformed into a body-fixed rotating and translating frame of reference. Furthermore, the arbitrary Lagrangian–Eulerian method allows the usage of flexible meshes, which is essential in the context of fluid–structure coupling. Arbitrary relative motion of grid blocks is made possible by the Chimera technique of overlapping grids. Further information on the code can be found in [24,25]. For aeroelastic computations, a robust algebraic grid deformation tool using Hermite polynomials [26] is applied before each time step, to update the structured aerodynamic mesh according to the surface-deformation description provided by the structure solver. The deformed surface is determined by bending and twisting the blade quarter-chord line.

For the present study, we use the Jameson second-order central scheme, due to its high robustness. The implicit dual-time-stepping scheme is used for the physical time integration, because it is best suited for the computation of complex unsteady phenomena. For this reason, certain FLOWer features (e.g., the deforming-mesh interface) are only usable in conjunction with the dual-time-stepping scheme. The computations were carried out using either the Baldwin–Lomax turbulence model or the Menter $k\omega$ shear stress transport (SST) model. Further information on the choice of the turbulence model is given in Sec. V.

## III. Weak Coupling Strategy

The idea of the weak coupling scheme is as follows: HOST uses CFD loads to correct its internal 2-D aerodynamics and retrims the rotor. The blade dynamic response is introduced into the CFD

calculation to obtain updated aerodynamic loads. This cycle is repeated until the CFD loads match the blade dynamic response evoked by them. A criterion for this converged state is given by the change of the collective and cyclic pitch angles with respect to the preceding cycle. Convergence is reached after the changes in these free-control angles have fallen below an imposed limit. The specific steps of the coupling procedure are thus given as follows:

1) HOST determines an initial trim of the rotor based on its internal 2-D aerodynamics derived from airfoil tables. The complete blade dynamic response for a given azimuth angle is fully described by the modal base and the related generalized coordinates.

2) The blade dynamic response is taken into account in the succeeding CFD calculation by the reconstruction of the azimuth-angle-dependent blade deformation from the modal base and by the respective grid deformation of the blade grid.

3) The CFD calculation determines the 3-D blade loads (forces and moments at each radial station) in the rotating rotor hub system. The loads are provided to HOST as load distributions (sectional lift, drag, and pitching moments) along the blade span for every azimuth angle.

4) For the next trim, HOST uses a load given by

$$\bar{F}^{\,n}_{\mathrm{HOST}} = \bar{F}^{n}_{2D} + \bar{F}^{n-1}_{3D} - \bar{F}^{n-1}_{2D} \tag{2}$$

where $\bar{F}^{n}_{2D}$ represents the free parameter for the actual HOST trim. A new dynamic blade response is obtained, which is expressed by an update of the generalized coordinates.

5) Steps 2 to 4 are repeated until convergence has been reached (i.e., when the difference

$$\Delta\bar{F}^{n} = \bar{F}^{n}_{2D} - \bar{F}^{n-1}_{2D} \to 0 \tag{3}$$

tends to zero and the trim loads depend only on the 3-D CFD aerodynamics).

It is mandatory that the updated CFD loads for each successive trim are periodic with respect to the azimuth angle. After the CFD calculation has been restarted from the previous run, a certain number of time steps (i.e., a certain azimuth angle range) is necessary until the perturbation introduced by the updated set of generalized coordinates has been damped down and a periodic answer is obtained again. Clearly, this state is reached more quickly when the initial disturbance is smaller. For this reason, the azimuth angle range covered by the CFD calculation can be reduced with an increasing number of retrims. The changes in the free controls and the blade dynamic response become smaller from one retrim to the next.

## IV. Vortex-Tracking Methodology

The intention for the usage of vortex-adapted grids is to provide a local refinement of the mesh only in the region in which it is actually needed (i.e., in the vicinity of the tip vortices). This refinement is achieved by adding additional tube-shaped grids to the existing Chimera grid setup. In comparison with alternative approaches (e.g., the local refinement of the Cartesian background grid), vortex-adapted grids have the advantage to be topologically well adapted to the tip vortices. The method of vortex-tracking Chimera grids has been previously used by, amongst others, Egolf et al. [2], Hariharan [27], and Lee and Baeder [28]. The strategy presented in this work is comparable, but the method is directly applied to a trimmed rotor in BVI flight condition. As for the references mentioned, it is assumed that a dominating tip vortex is shed from the blade tip, which can be captured by the vortex-tracking grid. There is no special treatment of a spread vortex sheet that might be shed along the blade span. The idea is that the interaction of distinct tip vortices with the blade is by far the most predominant source of BVI noise. Hence, we expect to achieve a significant improvement with this technique.

As already stated, our method adds vortex-adapted grids to the existing Chimera grid setup. This standard Chimera system consists of a Cartesian off-body (or background) grid and four body-conforming near-body grids of C topology surrounding the blade surface. Four vortex-adapted grids are embedded into this grid system, each of them being associated with one of the blade grids. To correctly capture the tip vortex, two aspects have to be accounted for, as follows:

1) The location of the vortex grid has to be adapted to the vortex position.

2) The flow transfer between vortex grids, background grid, and blade grid has to be handled.

These aspects will be discussed in the following sections.

### A. Vortex-Grid Generation

In the case of a forward-flight configuration, the position of the tip vortex relative to the rotor hub varies with time as the vortex is convected downstream. Therefore, the position of the vortex-adapted grid has to be adapted every physical time step of the unsteady computation to fit the current position of the vortex. We use the following strategy: The vortex grid covers a certain wake age of the vortex, starting behind the blade tip of the corresponding blade. At the beginning of a new physical time step, the vortex-grid coordinates are updated by shifting the grid into its new position. The shape of the grid varies from one time step to the next, as another sector of the helical trajectory is covered by the grid. Thus, the grid coordinates of a given time step cannot be transferred to the coordinates of the following time step using a pure rigid body shift. In fact, the vortex-adapted grid has to be treated as a deformable grid. FLOWer provides a comfortable interface for the treatment of deforming meshes. The code needs only to be provided with the updated grid coordinates, and all related actions (computation of new metrics under consideration of the geometric conservation law, whirl fluxes, and source terms) are performed by FLOWer.

#### 1. *Vortex-Grid Centerline*

To set the coordinates of the vortex-adapted grids, the grid centerline has to be defined. We use an analytical approach for the definition of this centerline, which ideally should match the actual vortex trajectory. A first approximation for the vortex trajectory is obtained from the path, which is covered by the blade tip. In the nonrotating rotor hub system, this path is given by the following equations:

Longitudinal coordinate:

$$\frac{x}{R} = \cos(\psi_w - \psi) + \mu \cdot \psi_w \tag{4a}$$

Lateral coordinate:

$$\frac{y}{R} = -\sin(\psi_w - \psi) \tag{4b}$$

Axial coordinate:

$$\frac{z}{R} = -\lambda \cdot \psi_w = -\frac{V \cdot \sin\alpha_q}{\Omega \cdot R} \cdot \psi_w \tag{4c}$$

where $\lambda$ is denoted as the rotor inflow angle. Of course, these equations yield only a raw approximation for the actual position of the vortex. This set of equations purely describes the convection of the rotatory motion due to the translatory forward-flight motion, resulting in the typical helical shape. The actual position of the vortex is affected by the rotor downwash (i.e., the distribution of the induced velocity in the rotor wake). A first attempt to take the rotor downwash into account was performed by simply assuming a constant distribution of the induced velocity on the rotor disk. An approximation for the induced velocity can be obtained from jet theory using the mean value of the rotor thrust coefficient. In this case, the additional contribution to the rotor inflow angle can be approximated as follows:

$$\lambda = \frac{V \cdot \sin\alpha_q + v_i}{\Omega \cdot R} \approx \frac{V \cdot \sin\alpha_q}{\Omega \cdot R} + \frac{C_T}{2\mu} \tag{5}$$

We used this approximation for the computation of fast forward-flight cases with a positive (nose-down) rotor shaft angle. In this case, the vortices are located below the rotor disk and no interaction with

the blades occurs. For such cases, the preceding approximation turned out to be sufficient to keep the tip vortex in a vortex grid with the cross-sectional dimension of $2.5 \times 2.5$ blade chords for about 1.5 rotor revolutions. However, for the slow-descent flight case discussed in the present paper, this approach is not accurate enough. Because of the nose-up tilt of the rotor shaft, the component of the far-field velocity in the hub direction is directed upwards, whereas the induced velocity of the rotor is directed downwards. This results in a nonuniform velocity distribution on the rotor disk, leading to increasing distortions of the vortex trajectory with increasing wake age. Thus, using the preceding definition of the vortex-grid centerline, the tip vortex will not be contained in the vortex grid for the complete wake age range covered by the grid, but it leaves the vortex grid at higher wake ages. One possibility to overcome this problem could be to correct the position of the vortex grid using an automatic detection of the vortex center. However, for a BVI flight case, the tip vortices interact with each other and with the rotor blades. In these interaction regions, the vortex does not show an "ideal" vortical structure, but it may be distorted or separated into smaller vortical structures. Therefore, we expect that an automatic detection of the vortex centerline would not provide reliable results.

Our current approach uses an analytical description for the distortion of the vortex trajectory and is based on the semi-empirical results of Egolf and Landgrebe [29], who suggested using an envelope function and a shape function to describe the distortion of the vortex trajectory from the basic relations given earlier. The envelope function is used to describe the amplitude of the distortion, whereas the shape of the distortion is given by the shape function. We use this approach both for the distortion of the trajectory in the radial (in-plane) and axial (hub) directions. The distortion at a given location is obtained by multiplying the shape function and the envelope function:

$$\begin{aligned} \Delta z &= E_{\mathrm{ax}} \cdot S_{\mathrm{ax}} \\ \Delta r &= E_{\mathrm{rad}} \cdot S_{\mathrm{rad}} \end{aligned} \tag{6}$$

We use a linear approach for the shape function and a Fourier series approach for the envelope function:

$$\begin{aligned} E &= c \cdot \psi_w \\ S &= a_0 + \sum_{i=1}^{n} (a_{iS} \cdot \sin i\bar{\psi}_w + a_{iC} \cdot \cos i\bar{\psi}_w) \end{aligned} \tag{7}$$

The envelope function is a pure function of the wake age, whereas the shape function depends on the phased wake age $\bar{\psi}_w$, which is defined as the difference between the wake age $\psi_w$ of a point on the tip vortex and the azimuth position of the blade from which it was shed, $\psi$. Naturally, the coefficients $c$, $a_0$, $a_{iS}$, and $a_{iC}$ are not known in advance and have to be adapted to fit the actual tip vortex trajectory. We applied the following technique to determine the unknown coefficients: First, a provisional computation using vortex grids based on the undistorted trajectory [Eq. (4)] with a comparatively large cross-sectional extension of the vortex grid is performed. Then, for a certain blade azimuth angle, the vortex center locations within the corresponding vortex grid can be extracted interactively from the flow solution. From this information (vortex center location offset versus wake age and vortex center location versus phased wake age, respectively), the envelope function coefficient can be obtained by linear regression, whereas the coefficients of the shape function are obtained by a Fourier decomposition. A Fourier decomposition using six harmonics turned out to take into account all major distortion effects while still providing a "smooth" distribution. In Fig. 2, the undistorted and the distorted tip trajectories of the present test case are compared with each other. The effect of the envelope function and the shape function can clearly be seen from the distortion amplitude and the shape. It turned out that the result is not sensitive to the choice of the blade azimuth angle, which is chosen for the determination of the coefficients. This means that if a good approximation for the vortex trajectory was obtained for an arbitrary azimuth angle, then this approach holds for all blade azimuth angles. This also substantiates the validity of the approach.

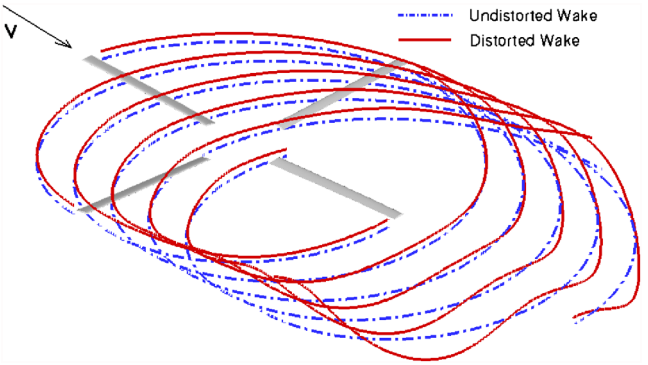


**Fig. 2 Comparison of undistorted (dashed) and distorted (solid) vortex trajectory.**

### 2. *Cross-Sectional Topologies*

Figure 3 shows the three types of cross-sectional topologies that were implemented into FLOWer: a Cartesian-based topology (Fig. 3a), a cylinder-based topology (Fig. 3b), and a combination of both, that is, a Cartesian-based core region surrounded by a cylindrical topology (Fig. 3c). The Cartesian-based grid section can be defined as a Cartesian mesh with a rectangular boundary or its boundary may be distorted toward a more circular shape, as shown in Fig. 3a. For all topologies, the outer extension of the cross-section, the number of grid cells and the grid clustering can individually be defined. We used the Cartesian-based topology for all computations of the present paper. Although at first view one might think that the cylinder-based grid section is better adapted to the vortex topology, this is only the case if the vortex is perfectly centered within the grid. In contrast to that a deviation of the actual vortex center and the grid section center is noncritical in the case of the Cartesian-based topology. A compromise between these two requirements (adaption to the vortex topology and tolerance with respect to a deviation of the vortex center) is provided by the two-block topology shown in Fig. 3c. The topology in Fig. 3a has proven best and was therefore

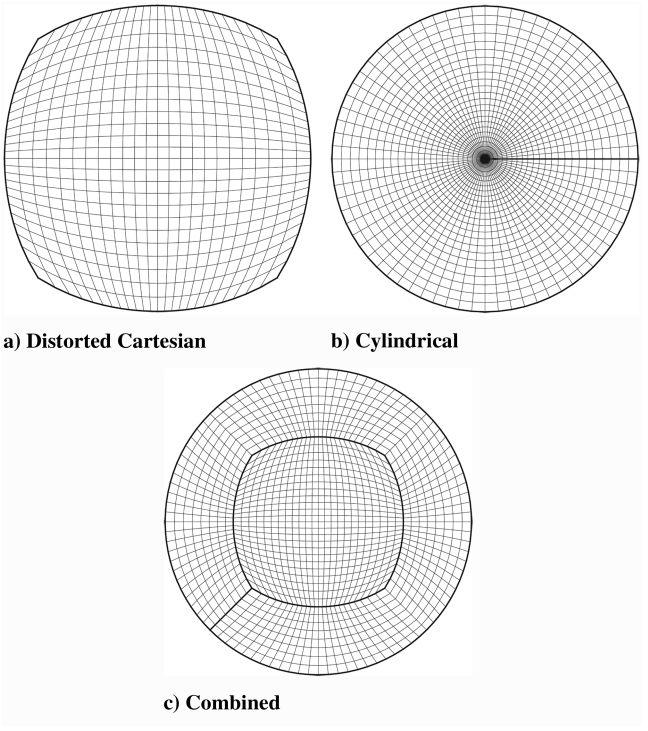


**Fig. 3 Possible cross-sectional topologies.**

used for all computations presented in this paper. The actual number of cross-sectional grid points used in the computations will be given in Sec. V.

The vortex-grid centerline is prescribed by the distorted wake equations given by Eqs. (4), (6), and (7). Because this approach is only an approximation of the actual vortex trajectory, the vortex location may slightly differ from the vortex-grid section center. To keep the tip vortex in the vortex grid, the outer dimensions of the cross section have to be large enough to tolerate this scatter in the vortex center location.

Furthermore, as we will show in the following section, a certain minimum dimension of the cross section has to be provided for Chimera reasons. An outer dimension of the vortex-grid section of $2 \times 2$ to $3 \times 3$ blade chords has proven to fulfill these requirements.

With the definition of the vortex-grid centerline and the cross-sectional grid topology, all information has been provided to generate the vortex-adapted grids. To allow for an effective parallelization of the flow computation, the vortex-grid structures are split into several grid blocks along the vortex-grid axis. This means that every grid block covers a certain wake age range. The flow transfer from one vortex-grid sector to the following is performed using block-cut boundary conditions.

### B. Chimera Treatment

The vortex-adapted grids are embedded into the existing grid system, which consists of a Cartesian background grid and four curvilinear blade grids. The flow exchange between the different grid structures is established by the Chimera technique [25]. For the standard Chimera setup (i.e., if no vortex-adapted grids are present), the flow exchange is performed as follows: The outer block boundary of a blade (or near-body) grid structure is defined as a Chimera boundary and the flow condition at the boundary is obtained from the background (or off-body) grid by Chimera interpolation. In the other direction, data transfer from each blade grid into the background grid is performed by interpolation on the boundary points surrounding a hole area cut into the background grid. For this purpose, a cylindrical hole is defined that completely surrounds the respective rotor blade. All cells of the background grid located within this cylinder are blanked out and the cells of the background grid surrounding the cylinder are marked off for interpolation. These cells obtain their flow condition by interpolation from the blade grid. FLOWer uses two Chimera fringe layers covering the full stencil of the available spatial schemes.

In the case of the usage of vortex-adapted grids, the flow exchange between the vortex grids and the other grid structures has to be established. The following aspects have to be addressed:

1) The blade-tip vortex has to be transferred into the corresponding vortex-adapted grid.

2) The flow exchange between the vortex-adapted grids and the background grid has to be established.

3) In the case of interaction of a vortex with a blade, the flow transfer from the vortex grid into the blade grid and back has to be ensured.

The first item is addressed by the interpolation of the flowfield from the blade grid onto the front face of the vortex-adapted grid. This situation is depicted in Fig. 4a. The front face of the vortex grid is located behind the blade tip of the corresponding blade, with a few degrees offset in the wake age direction from the actual blade tip. The tip vortex is created in the blade grid and is transferred into the vortex grid via the Chimera block boundary of its front face. The location of the blade tip in the rotating system varies with time as the elastic blade is subject to flap motion and deformation. The cross-sectional dimension of the vortex grid of approximately $2 \times 2$ to $3 \times 3$ blade chords is large enough to cover the flap deflection range of the blade tip.

By default, all other block boundaries of the vortex-adapted grid obtain their boundary condition by Chimera interpolation from the background grid. But without an additional treatment, the boundary condition provided by the background grid would be purely based on the vortex conservation properties of the background grid, which are poorer than the vortex conservation provided by the vortex grid. This can be corrected by the retransfer of the flow solution from the vortex grid into the background grid. Thus, for every vortex grid, an additional hole has to be cut into the background grid. In FLOWer, hole regions of arbitrary shape may be defined by providing auxiliary grids as hole-defining grids. One straightforward way of obtaining such a hole-defining grid would be to simply restrict the cross-sectional extension of the vortex grid using some interior circumferential grid line as the new outer grid boundary. However, the resulting hole-defining grid would be a very fine grid, leading to a unnecessarily high computational effort for the blanking process. This can be avoided by creating a coarse auxiliary grid as a hole-defining grid, obtained by scaling the sectional dimension of the vortex-adapted grid by a user-supplied scaling factor. A sectional grid resolution of the auxiliary grid of $2 \times 2$ grid points (one single cell) turned out to be sufficient for most configurations. Finally, the cells of the background grid located inside the hole-defining grid are blanked out and the grid cells surrounding the hole are updated using donor cells from the vortex-adapted grid.

Figure 4b shows the situation when a vortex-adapted grid intersects with a blade grid (i.e., when a tip vortex interacts with a rotor blade). In this case, the vortex has to be transferred from the vortex grid into the blade grid, and the interaction effect has to be retransferred from the blade grid into the vortex grid. The first aspect is treated as follows: By default, the blade grid obtains its boundary condition by Chimera interpolation from the background grid. Only for those boundary cells, for which an interpolation from a vortex-adapted grid is possible, will the respective vortex grid be explicitly searched for a donor cell. The retransfer of flow information from the blade grid into the vortex-adapted grid is performed by blanking cells of the vortex grid with the same cylindrical hole definition that is used for the blanking of the background grid.

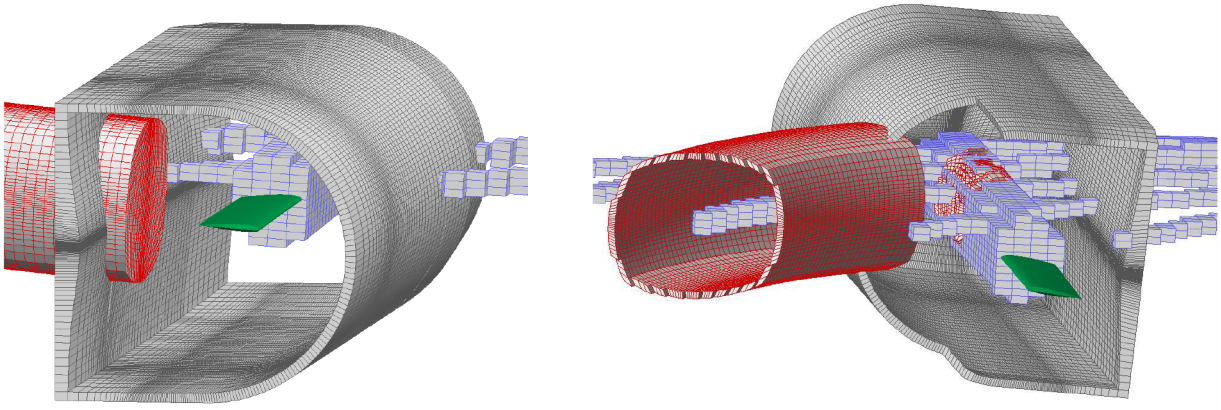

**a) Transfer of the tip vortex into the vortex-adapted grid** **b) Interaction of a vortex-adapted grid with a blade grid**

**Fig. 4 Chimera flow exchange.**

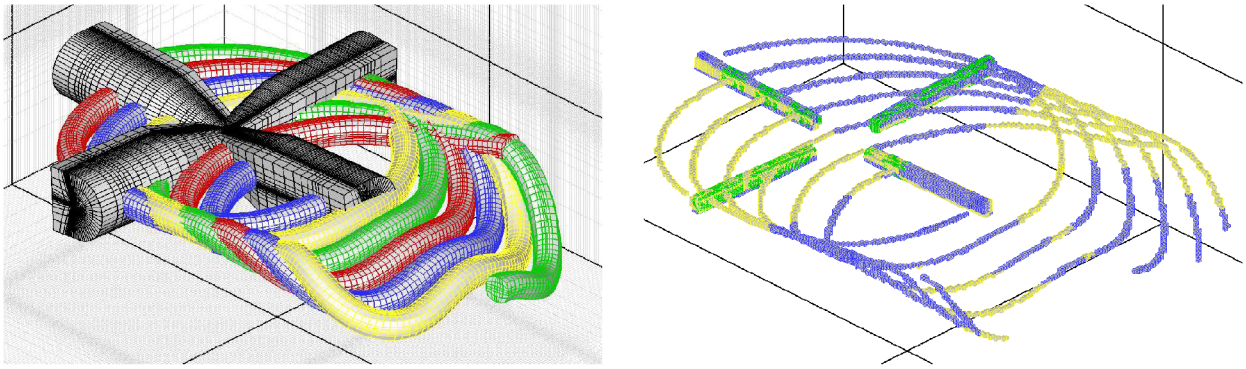

a) Grid system b) Hole system

Fig. 5 Chimera setup.

The resulting Chimera grid system and the related hole system are shown in Fig. 5. It can be seen that the application of vortex-adapted grids results in a comparatively complex Chimera setup that requires an effective treatment to keep the Chimera overhead for hole definition and donor cell search within an acceptable limit. The usage of a Cartesian background grid is mandatory for the present purpose, because for a Cartesian mesh, the axis directions are equivalent to the index directions and can thus be searched independently for a potential donor cell. Naturally, this search method is much faster than the alternating digital tree (ADT) method that FLOWer applies for the donor cell search in non-Cartesian meshes. Therefore, the time-consuming ADT search is only performed for those Chimera target points that were marked for the search in a non-Cartesian block and for those target points for which no valid donor cell could be found in the Cartesian background grid. This means that vortex-adapted grids are not usually searched for donor cells to update target points located on other vortex grids, because this would be too time-consuming. Instead, the flow exchange is established via the background grid and the search for a donor cell in other vortex grids is only done if, for the present target point, no valid donor from the background grid is available. This is automatically the case if two or more vortex-adapted grids overlap. In this case, donors are searched in the other vortex-adapted grids, which guarantees an accurate flow exchange between the vortex grids.

For a typical test case using vortex-adapted grids, approximately 30% of the computational effort of a physical time step is required for the Chimera setup process and about 70% is required for flux computation. Without vortex-adapted grids, the Chimera overhead reduces to approximately 17%. Thus, the increase in Chimera is still acceptable. However, as already stated, the usage of a Cartesian background grid and the selective search procedure is mandatory. Otherwise, the benefits of the method would be swept off by the too-large Chimera overhead.

It should be noted that the grid resolutions and the cross-sectional extensions of the vortex grids and the hole-defining auxiliary grids have to be adapted to each other to minimize the number of Chimera orphan points (Chimera target points for which no valid donor cell is available). Orphan points should be avoided both for accuracy and performance reasons. If these parameters are thoroughly chosen, a Chimera setup without any Chimera orphan points can easily be provided.

From the preceding explanations, it can be seen that a lot of care was taken in establishing an accurate flow transfer between the individual grids, while at the same time speeding up the search procedure as much as possible. The risk of generating unphysical solutions by an inadequate flow exchange was thus minimized.

## V. Results and Discussion

For the present paper, we restricted our investigations to the HART-2 baseline case, which features a pure monocyclic pitch input, and to the first of the two HHC cases, the minimum-noise case. For these cases, we will discuss the CFD/CSD coupled trim analysis and we will compare the prediction of BVI for different grid setups. The computational results will be compared with the experimental data.

### A. Descending Forward-Flight Conditions

The HART-2 test uses a 40% Mach-scaled, four-bladed, hingeless Bo105 model rotor. It is dynamically scaled to match the natural frequencies of the full-scale blade in the first three flaps, first two lead lags, and first torsion modes. The rotor blades are rectangular with a −8-deg linear twist and a precone angle of 2.5 deg. The blade features a modified NACA23012 airfoil with a trailing-edge tab of 5.4-mm length and 0.8-mm thickness. The hover tip Mach number is 0.64 and the advance ratio is 0.15. The rotor was installed with a rotor shaft angle of 5.3 deg (nose-up). For the computation, we prescribed a shaft angle of 4.5 deg, taking 0.8 deg of wind-tunnel interference effect into account. The minimum-noise case is obtained from the baseline case by introducing an additional three-per-revolution cyclic pitch control with an amplitude of $\theta_{3/\mathrm{rev}} = 0.8$ deg and a phase of $\psi_{3/\mathrm{rev}} = 300$ deg. The data are summarized in Table 1.

### B. Trim Convergence and Blade Dynamics

The coupled CFD/CSD computations were trimmed for the experimental values of thrust $F_z$, rotor mast rolling moment $M_x$, and rotor mast pitching moment $M_y$ by the adaption of the free-control angles $\theta_0$, $\theta_c$, and $\theta_s$. The rotor shaft angle was held fixed at the effective value of 4.5 deg. The rotor trim was performed with a standard grid setup (i.e., without the application of vortex-adapted grids), assuming that the effect of an improved vortex conservation on the rotor trim is negligible.

Table 2 contains the grid sizes used for the rotor trim. We used a comparatively coarse background grid with only 1.8 million grid cells and a grid spacing of approximately 0.25 blade chords in the rotor disk area. The blade grids use a C-mesh topology. At the blade root and the blade tip, the blade surface is contracted toward a cut condition. Because of restrictions of the grid deformation algorithm, the insertion of an additional block behind the blade trailing edge for an improved treatment of the finite trailing-edge thickness was not possible. Therefore, the mesh had to be closed to a cut at the trailing edge. In this case, the accurate reproduction of the tab geometry leads

Table 1 Descending forward-flight conditions

| Test case | $\mu$ | $\alpha_q$ | $Ma_{\mathrm{Tip}}$ | $\theta_{3/\mathrm{rev}}$ | $\Psi_{3/\mathrm{rev}}$ | $F_z$ | $M_y$ | $M_x$ |
|---|---|---|---|---|---|---|---|---|
| Baseline | 0.15 | 4.5 deg | 0.64 | —— | —— | 3300 N | −20 Nm | 20 Nm |
| Minimum noise | 0.15 | 4.5 deg | 0.64 | 0.8 deg | 300 deg | 3300 N | −30 Nm | 30 Nm |

**Table 2 Grid setup used for the trim computation**

| | Blade grids (no tab) | Blade grids (incl. tab) | Background grid |
|---|---|---|---|
| Grid dimension | $4 \times 149 \times 57 \times 81$ | $4 \times 233 \times 57 \times 81$ | $65 \times 145 \times 193$ |
| Number of cells | $4 \times 663,404$ | $4 \times 1,039,360$ | $1,769,472$ |

to distorted grid cells in the tab region. For this reason, it was decided to perform a preliminary investigation for the baseline case, neglecting the trailing-edge tab. The flow computation was performed using the Baldwin–Lomax algebraic turbulence model and a time step of 1.0-deg azimuth. Figure 6a shows the convergence of the control angles $\theta_0$, $\theta_c$, and $\theta_s$ for the weak coupling process. Although the control angles are in good agreement with the experimental values, the trim convergence of the lateral cyclic pitch angle $\theta_s$ is not satisfying. After six retrims, the changes both in collective pitch and longitudinal cyclic pitch have fallen below 0.01 deg, whereas the change in $\theta_s$ still exceeds 0.03 deg. The reason for this behavior can be seen from Figs. 6b and 6c. Figure 6b shows the elastic blade-tip torsion; the sectional pitching moment coefficient at 87% blade radius is given in Fig. 6c. The poor convergence in $\theta_s$ is caused by an unstable behavior of the blade. The elastic blade torsion implicates a pitching moment, which leads to an excitation of the elastic torsion, and so on. The agreement of the elastic blade torsion with the measurement gets poorer from one trim to the next. The trailing-edge tab obviously has a significant influence on the pitching moment gradient of the NACA23012 airfoil. This effect has also been observed for the full-scale blade [30]. It can be stated that an incorrect prediction of the pitching moment, combined with the low torsional stiffness of the Bo105 rotor, leads to a completely different aeroelastic behavior of the rotor.

Based on these results, the tab influence was investigated in more detail. A new blade grid was generated that takes into account the exact tab geometry. The blade surface mesh and the near-body C-mesh are shown in Fig. 7, and the grid resolution is given in Table 2. Furthermore, the question arises if the Baldwin–Lomax turbulence model is sufficient to capture the flow separation and vortex shedding effects caused by the tab or if a more sophisticated turbulence model has to be used. We compared the Baldwin–Lomax algebraic model and the $k\omega$-SST two-equation model, which is said to be well suited for flows with separation effects. In Fig. 8, the pressure distribution and the sectional pitching moment at 87% blade radius are compared for the blade dynamics of the zeroth HOST trim. As expected, the pressure distributions predicted by the two turbulence models do not match in the tab region. This implies differences in the prediction of the sectional pitching moment, as seen from Fig. 8b. We decided to use the $k\omega$-SST model for the trim computation and to switch back to the Baldwin–Lomax model for the investigations on vortex conservation, due to the higher robustness and the lower computational effort of the algebraic model.

In Fig. 9, the trim convergence for the control angles $\theta_0$, $\theta_c$, and $\theta_s$ is shown for the baseline case (Fig. 9a) and the minimum-noise case (Fig. 9b), taking into account the influence of the tab. It can be seen that the unstable behavior has disappeared and a trimmed state is now obtained after five retrims for both flight conditions. After five retrims, the changes in all control angles have dropped below 0.01 deg. Results for the blade dynamics of both flight cases are given in Figs. 10 and 11. The figures show the baseline case on the left-hand side and the minimum-noise case on the right-hand side. From the comparison of Figs. 6b and 10, it can clearly be seen that the elastic tip torsion was completely changed by taking the trailing-edge tab into account. The distribution of the tip torsion versus azimuth is now well-predicted, and the change in torsional behavior from the BL case to the MN case is well-captured by the coupled CFD/CSD method. It is conspicuous that the torsional mean value is clearly underpredicted by about 1 deg, both by the trimmed CFD/CSD solution and by the solution of the zeroth HOST trim. This is probably caused by a wrong (too much nose-down) mean value of the pitching moment. Test computations have shown that the mean

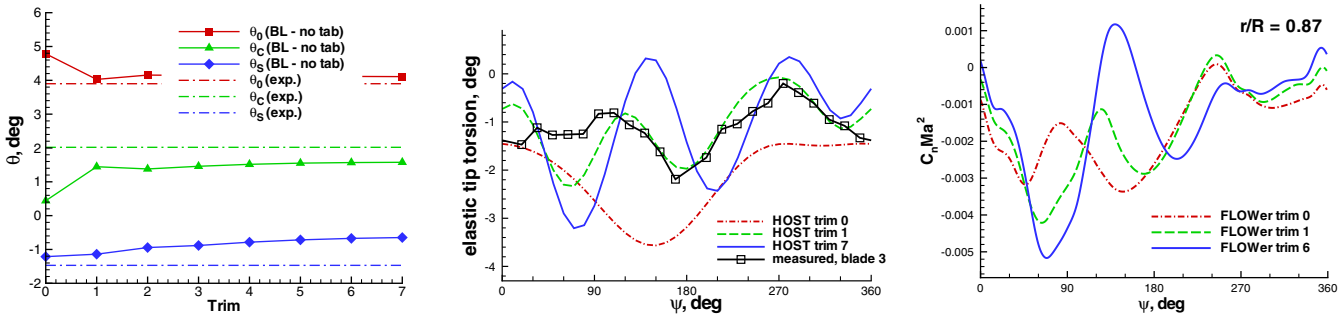


**a) Trim convergence** **b) Elastic torsion** **c) $C_m Ma^2$ at 87% blade radius**

**Fig. 6 Unstable aeroelastic behavior.**

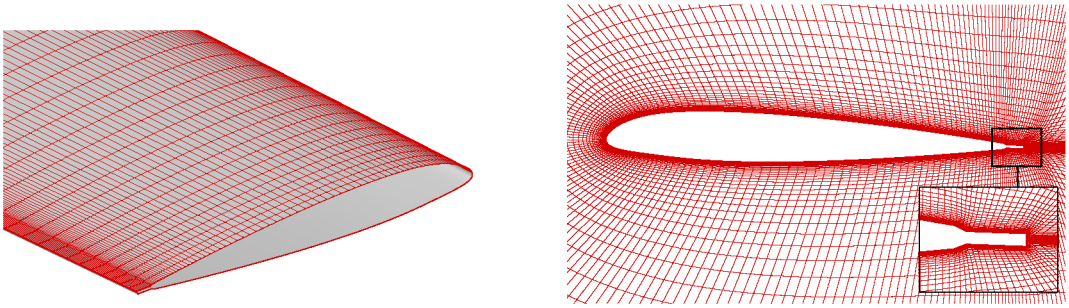

**a) Blade surface mesh** **b) Blade section C-mesh**

**Fig. 7 Blade surface mesh and blade grid section.**

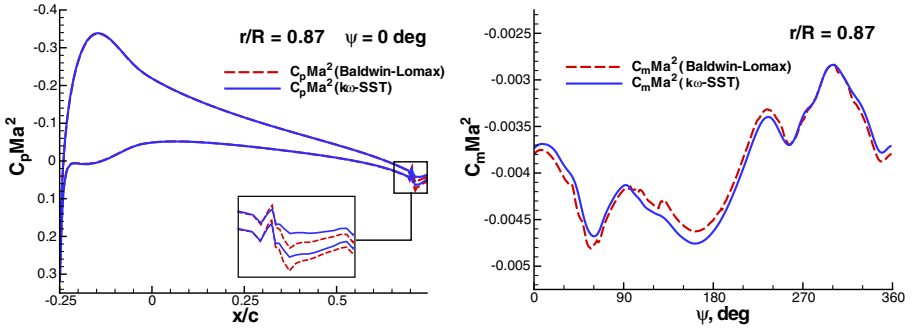


a) Pressure distribution b) $C_m Ma^2$ at 87% blade radius

Fig. 8 Influence of the turbulence model.

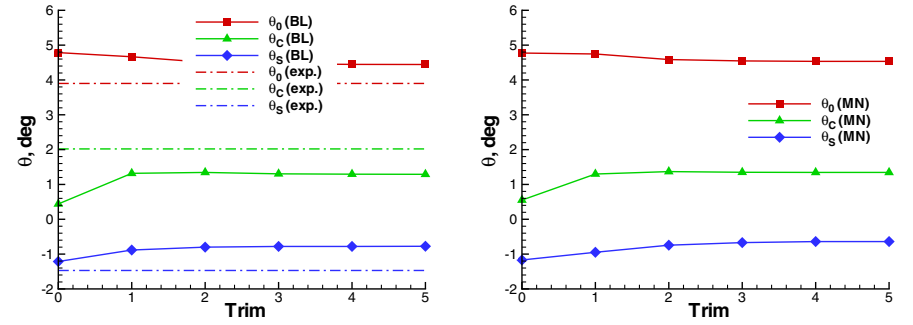


a) Baseline b) Minimum noise

Fig. 9 Trim convergence of control angles.

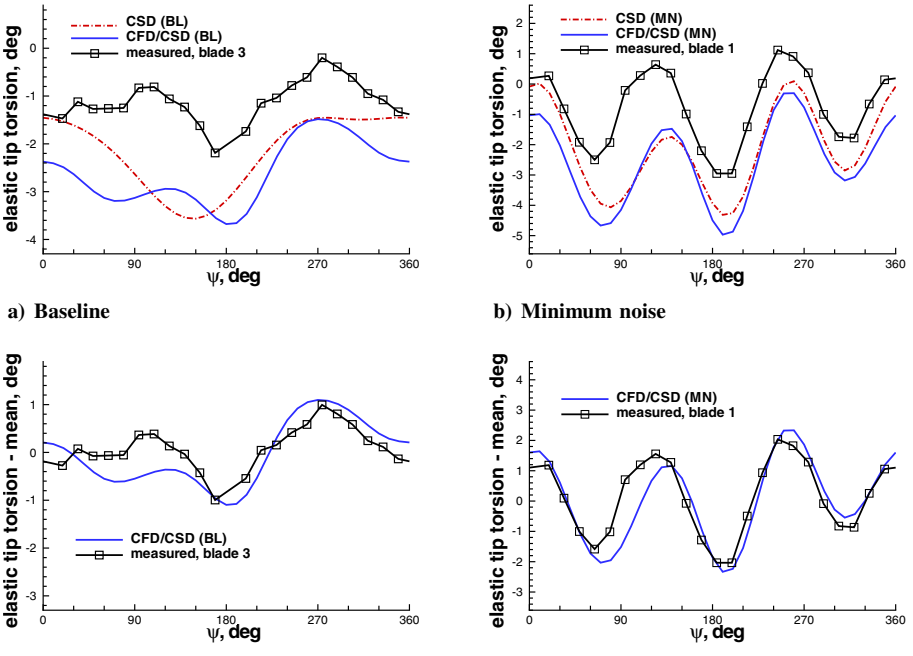


a) Baseline b) Minimum noise

c) Baseline, mean value corrected d) Minimum noise, mean value corrected

Fig. 10 Elastic blade-tip torsion.

value of the pitching moment is massively influenced by the tab angle with respect to the airfoil chord, which is defined as zero for the NACA23012mod airfoil. Even small changes in the tab angle in the range of ±0.25 deg have a considerable influence on the pitching moment. An improvement of the prediction of the torsional mean value will be subject to further investigations. For the present investigation, the deviation in the mean value is of minor interest, because the too-strong nose-down torsion is compensated by a higher collective pitch angle (the rotor is trimmed for thrust). For a better comparison of the torsional distribution with the experiment, the mean value was eliminated in Figs. 10c and 10d.

The blade-tip flapping amplitude versus azimuth (including precone) is given in Fig. 11. Again, in Figs. 11c and 11d, the mean value was eliminated. For both flight cases, the blade-tip flapping distribution is excellently predicted, but the mean value is again incorrect. At first glance, this is remarkable, because the rotor was trimmed for the experimental thrust level. The too-low mean flapping amplitude is probably caused by the too-low (too much nose-down)

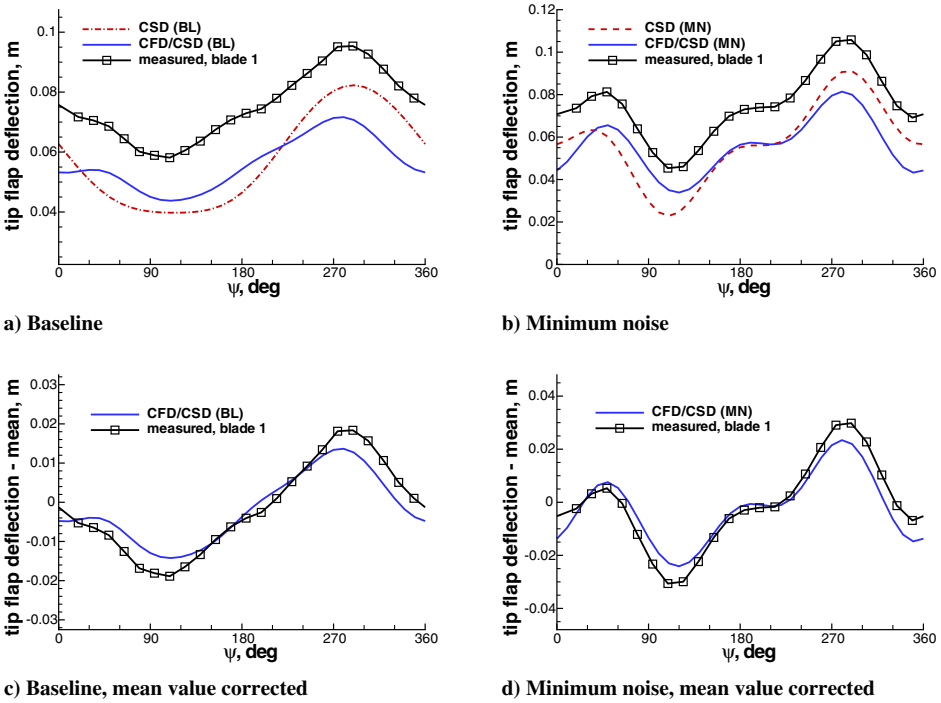


**a) Baseline** **b) Minimum noise**

**c) Baseline, mean value corrected** **d) Minimum noise, mean value corrected**

**Fig. 11 Tip flap deflection.**

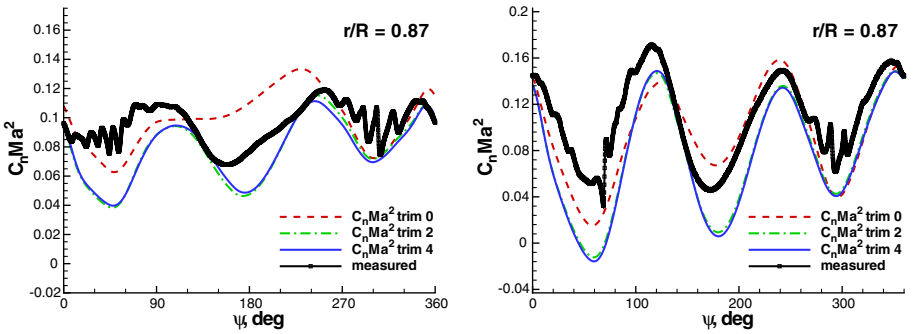


**a) Baseline** **b) Minimum noise**

**Fig. 12 Trim iteration history for $C_nMa^2$.**

mean value of the pitching moment. The pronounced nose-down elastic torsion of the blade, combined with the higher collective pitch, leads to a redistribution of rotor thrust from the outboard to the inboard region of the rotor disc. Accordingly, the flapping moment acting on the blade is reduced below the experimental value.

Figure 12 shows the development of the sectional normal force coefficient $C_nMa^2$ at 87% rotor radius for the baseline case (Fig. 12a) and the minimum-noise case (Fig. 12b). For both flight cases, a good overall agreement with the experiment can be observed. However, for the baseline case, the three-per-revolution character of $C_nMa^2$ is clearly overpredicted. The strongest deviations from the experiment can be seen on the advancing blade side, on which the experimental value is underestimated for both flight cases. Similar deviations from the experiment were observed in other numerical studies on this test case [31,32]. A better agreement could possibly be obtained by an improvement in the elastic torsion prediction. A lower nose-down elastic torsion will redistribute the rotor thrust toward the outboard region of the rotor disc, which should lead to higher sectional normal force coefficients, especially on the advancing blade side. At first sight, one might think that the agreement with the experiment is not improved from the initial HOST trim to the final coupled CFD/CSD solution. But one should keep in mind that the trimmed solution actually represents real physics; that is, the aerodynamic loads match the blade dynamic response evoked by them. In contrast to that, the flow solution based on the zeroth HOST trim is only a generic scenario with a prescribed blade motion.

### C. Vortex Grids Versus Refinement of the Background Grid

The grid system used for the rotor trim is too coarse to capture any BVI effects. For this reason, the grid system was modified both by using refined background grids and by the application of vortex-adapted grids. In the present section, we restrict ourselves to the results of the baseline case. A similar investigation was performed for the minimum-noise case. The conclusions made for the baseline case hold for the minimum-noise case as well. The results presented in this section were obtained by applying the trim condition and blade dynamics presented in the previous section. For time and stability reasons, we switched back to the Baldwin–Lomax turbulence model. Furthermore, the Baldwin–Lomax model should be better suited for the purpose of vortex conservation, because one major drawback of the $k\omega$-type models is the high level of viscosity in vortical structures. Nevertheless, the results for $C_nMa^2$ may be compared with those obtained with the $k\omega$-SST model, because the sectional normal force is virtually unaffected by the choice of the turbulence model. In the following, three different grid arrangements will be compared: 1) vortex-adapted grids added to the standard grid setup, 2) grid setup using a medium background grid, and 3) grid setup using a fine background grid.

The medium background grid features a grid spacing of 0.18 blade chord in the rotor disc area. For the fine background grid, the grid spacing was reduced to 0.1 chord. The vortex-grid setup uses four vortex-adapted grids with a sectional grid spacing of 0.1 chord and an axial grid spacing of 0.5-deg wake age. The vortex grids feature a

**Table 3 Grid resolutions for the three grid setups investigated**

| | Blade grids | Background (coarse) | Background (medium) | Background (fine) | Vortex grids |
|---|---|---|---|---|---|
| Grid dimension | $4 \times 233 \times 57 \times 81$ | $65 \times 145 \times 193$ | $113 \times 209 \times 281$ | $105 \times 353 \times 409$ | $4 \times 33 \times 33 \times 1081$ |
| Number of cells | $4 \times 1,039,360$ | 1,769,472 | 6,522,880 | 14,936,064 | $4 \times 1,105,920$ |
| Grid resolution | —— | 0.25 chord | 0.18 chord | 0.1 chord | $0.1c \times 0.1c \times 0.5$ deg |
| Grid setup 1 | X | X | —— | —— | X |
| Grid setup 2 | X | —— | X | —— | —— |
| Grid setup 3 | X | —— | —— | X | —— |

distorted Cartesian topology with a sectional extension of $3 \times 3$ blade chords. A wake age of 540 deg (1.5 rotor revolutions) is covered by the grids. The grid data are summarized in Table 3. For all computations, a time step of 1-deg azimuth was applied.

In Fig. 13, the $C_nMa^2$ distributions at 87% rotor radius, predicted by the three different grid setups, are compared with the experiment. BVI effects can be seen on the retreating blade side in the azimuth range from 250 to 340 deg. The BVI is completely missed on the advancing blade side. Comparing the different grid setups, the vortex-grid setup 1 provides the best reproduction of the BVI oscillations, considerably better than for setup 2, which features a similar amount of grid cells. To obtain a comparable BVI prediction by a refinement of the background grid, the overall number of grid cells has to be doubled (grid setup 3). Although (at least on the retreating blade side) phase and direction of the BVI oscillations are correctly predicted, the amplitudes are massively underpredicted, even by grid setup 1. This may either be caused by a too-coarse grid resolution and thus an insufficient vortex conservation, or by a too-large time step of the flow computation. One has to keep in mind that the BVI is a highly unsteady phenomenon, because the vortex approaches the blade with its axis directed parallel to the blade. The choice of the time step should be less critical as long as the vortex is contained in the vortex-adapted grid, because the grid moves with the vortex. However, when the vortex is transferred from the vortex-adapted grid into the blade grid, the vortex location within the blade grid changes with time as the vortex approaches the blade.

Based on grid setup 1, we investigated the influence of a time-step reduction on the results. The time step was reduced to both 0.2-deg azimuth and 0.1 deg, leaving all other parameters unchanged. The results for $C_nMa^2$ are compared in Fig. 14. It can be seen that the change in the BVI amplitudes on the retreating blade side is negligible. However, both the 0.2-deg computation and the 0.1-deg computation reveal small BVI effects on the advancing blade side that were not captured by the 1-deg resolution. Otherwise, almost no differences are noticed between the 0.2-deg computation and the 0.1-deg computation. Thus, any further improvement of the solution by a further reduction of the time step seems unlikely. In [32], the BVI was well captured with a similar grid resolution (0.1 chord in the off-body grid) and a comparable time step. However, a fourth-order scheme in space was used in combination with inviscid modeling in the background grid. Because FLOWer uses only a second-order scheme in space, a considerably higher resolution will be necessary to obtain similar vortex conservation properties.

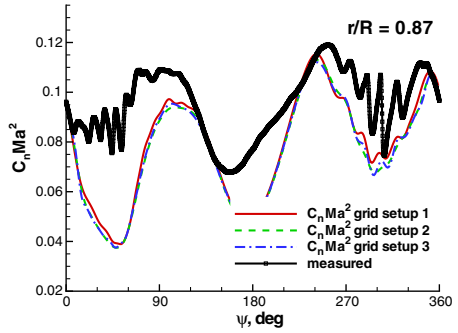


**Fig. 13 Grid setup influence on $C_nMa^2$.**

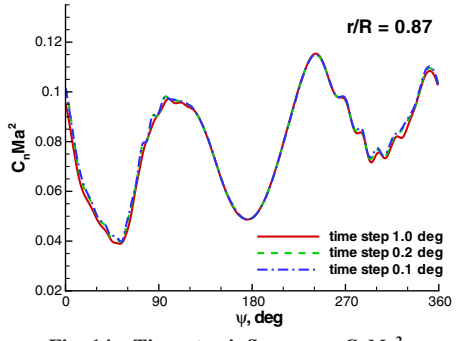


**Fig. 14 Time-step influence on $C_nMa^2$.**

### D. Grid Refinement

Using vortex-adapted grids, the grid resolution in the vicinity of the vortex can easily be increased by adding additional grid cells to the vortex-adapted grids. We increased the sectional grid resolution from $32 \times 32$ grid cells (0.1-chord spacing) to $64 \times 64$ cells (setup 4, 0.05-chord spacing) and $128 \times 128$ cells (setup 5, 0.025-chord spacing). To provide a comparable grid resolution at the Chimera boundary of the blade grids, the grid spacing of the blade grids was adapted by increasing the number of grid points. The grid data of the two setups are given in Table 4. The overall number of grid cells is approximately 24 million for grid setup 4 and 65 million for setup 5. Note that inviscid modeling was used for this refinement study.

A time-step size of 1-deg azimuth was used for both flight cases. The results for $C_nMa^2$ at 87% rotor radius are given in Fig. 15. It can be seen that a significant improvement compared with the results of the previous section was achieved by the refinement of the grid. A clear amplification of the BVI oscillations is already observed for the 24-million-cell setup and, as expected, a further improvement is achieved by the 65-million-cell setup. For the latter, some BVI is now also captured on the advancing blade side. On the retreating blade side, the BVI amplitudes now reach the order of magnitude observed in the experiment, although the full amplitude is still not completely reached. However, these results are encouraging and clearly show the potential of vortex-adapted grids. If similar vortex conservation properties should be achieved by a refinement of the background grid, then an area of at least the size of $35 \times 35 \times 3$ blade chords would have to be covered with a grid spacing of 0.025 blade chord. This grid spacing would have to be provided in all axis directions, because the vortex can be arbitrarily oriented within the grid. This would finally result in an overall number of more than 230 million grid points, which is at the edge of feasibility even on modern computers. In addition, one has to take into account that with this amount of grid cells, only the rotor disc area (which is relevant for BVI prediction) is covered with the fine spacing. Using vortex-adapted grids, the tip vortices can be tracked up to very high wake ages.

Figure 16 shows a visualization of the BVI effects on the rotor disk. The difference in the sectional normal force $\Delta C_nMa^2$ between the result predicted by the fine grid setup 5 and the standard grid setup 1 is plotted on the rotor disk. Using this plot style, the BVI can easily be identified in the first and fourth quadrants of the disc. Although from Fig. 15, the BVI airloads seem to be less pronounced for the minimum-noise case, Fig. 16 shows that higher values in $\Delta C_nMa^2$ are actually obtained for the minimum-noise case. This can

**Table 4 Grid resolutions of the refined grid systems**

| | Blade grids | Background grid | Vortex grids | Total |
|---|---|---|---|---|
| Grid setup 4 | $4 \times 233 \times 57 \times 81$ | $65 \times 145 \times 193$ | $4 \times 65 \times 65 \times 1089$ | 23,752,704 |
| Grid setup 5 | $4 \times 233 \times 97 \times 161$ | $105 \times 353 \times 409$ | $4 \times 128 \times 128 \times 545$ | 64,841,728 |

also be identified from Figs. 17 and 18, in which both $C_nMa^2$ and $\Delta C_nMa^2$ are plotted at the radial blade stations $r/R = 0.5$, $r/R = 0.75$, and $r/R = 0.87$. These figures show that the computations also capture BVI airloads on the advancing blade side. However, especially for the minimum-noise case, the BVI airloads on the advancing blade side are harder to identify from a $C_nMa^2$ plot, due to the strong gradients in $C_nMa^2$.

Figure 19 shows the three-dimensional flowfield that was obtained from grid setup 5. We used the well-known $\lambda_2$ criterion [33] for the visualization of the vortices. A contour level of $\lambda_2 = -0.001$ was chosen for visualization. The vorticity in the $y$ direction is plotted onto the isosurface as a contour variable, showing the sense of rotation of the vortex with respect to the flight direction. As a result of the application of vortex-adapted grids, the tip vortices are excellently conserved up to the wake age of 1.5 rotor revolutions. This can be seen best in the area behind the rotor disc, in which the vortex core remains well concentrated without being weakened by dissipation effects. In Fig. 20, the $\lambda_2$ value is plotted as a contour variable onto axial sections of the vortex-adapted grid. From this representation, both the vortex conservation properties of the vortex grid and the vortex capturing capability by the grid distortion are demonstrated.

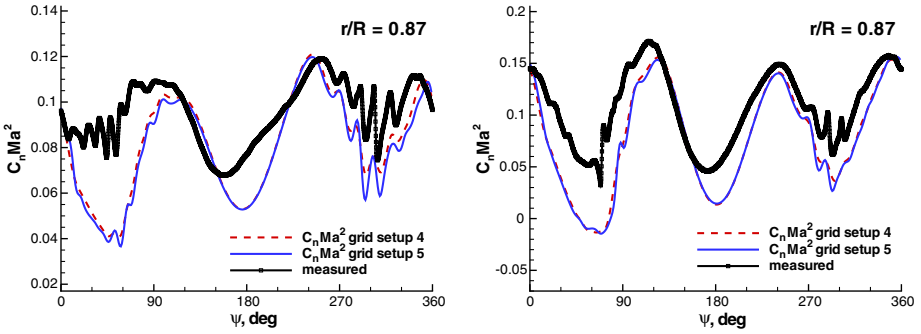


**a) Baseline** **b) Minimum noise**

**Fig. 15 $C_nMa^2$ prediction by refined grid setups.**

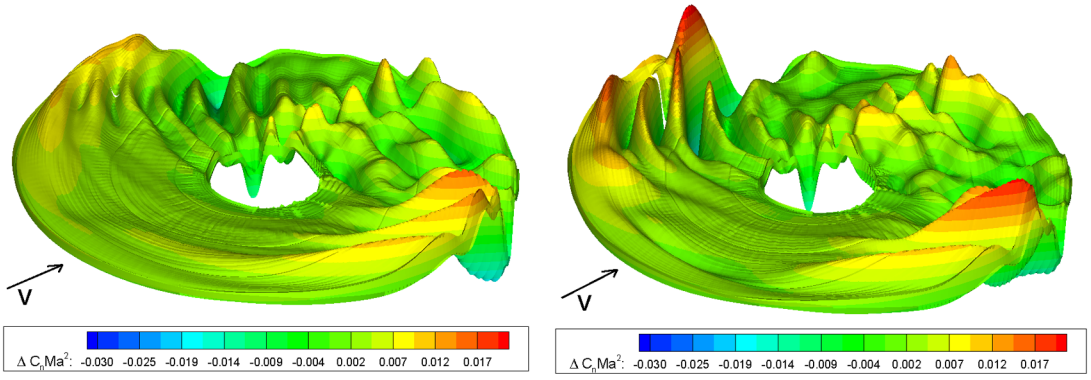


**a) Baseline** **b) Minimum noise**

**Fig. 16 Distribution of $\Delta C_nMa^2$ on the rotor disc.**

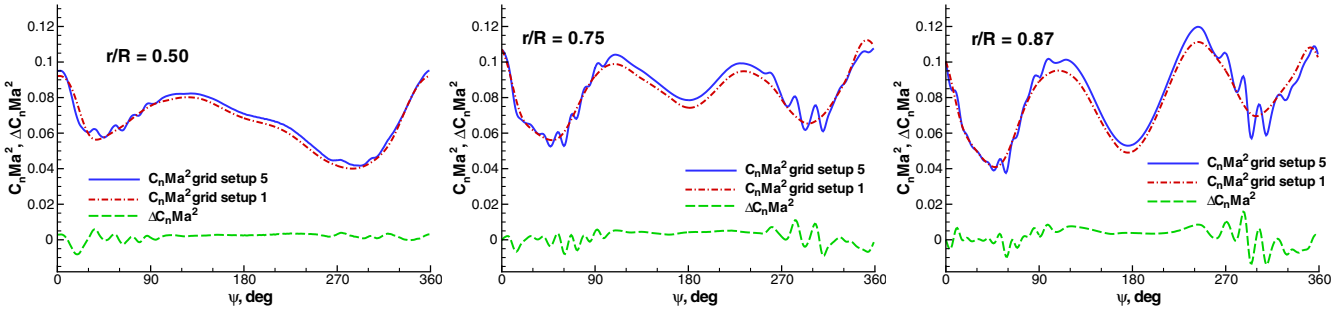


**a)** **b)** **c)**

**Fig. 17 $C_nMa^2$ and $\Delta C_nMa^2$ at selected radial stations (baseline case).**

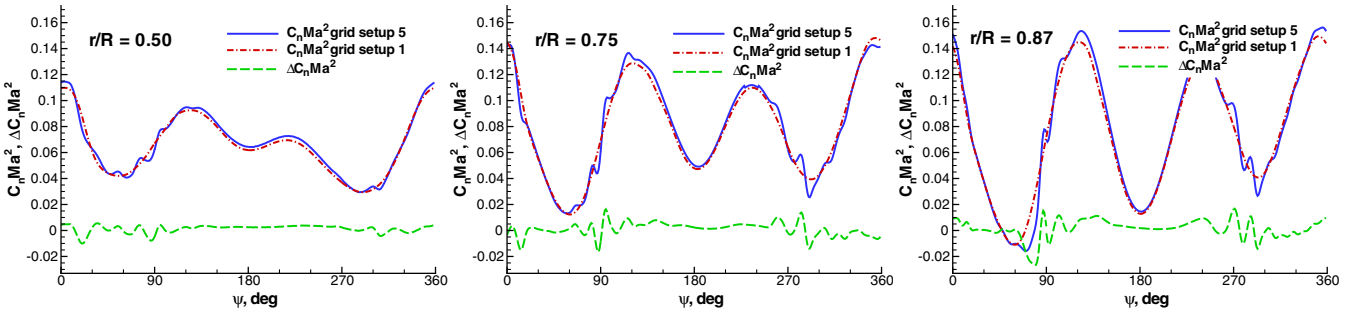


**Fig. 18 $C_nMa^2$ and $\Delta C_nMa^2$ at selected radial stations (minimum-noise case).**

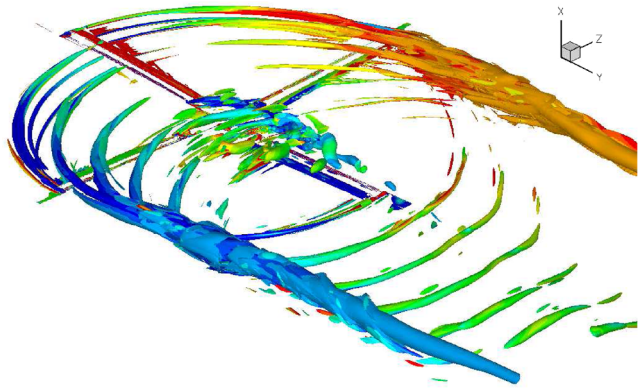

**Fig. 19 Visualization of the vortex system using the $\lambda_2$ criterion.**

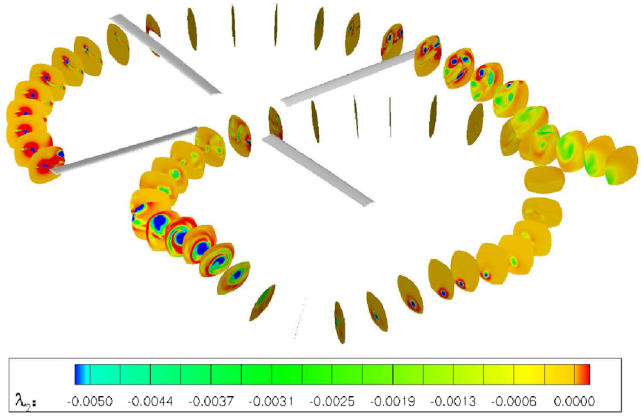


**Fig. 20 Contour of $\lambda_2$ on axial sections of the vortex-adapted grid.**

We have shown that vortex-adapted grids are a feasible way to capture and conserve the wake of a helicopter rotor in a CFD simulation. It is obvious that this technique cannot directly be transferred to other configurations in which the position of the vortices is not known in advance. However, one should keep in mind that the helicopter rotor wake is a very important type of flow that is of particular importance for several current research activities on helicopters (e.g., BVI noise reduction, evaluation of HHC and IBC control, and active rotor control). Vortex-adapted grids are a powerful tool to be applied on these problems.

## VI. Conclusions

We presented a method based on vortex-adapted Chimera subgrids to improve the tip vortex conservation in a CFD simulation. The method was applied to a main rotor in slow-descent flight, which is subject to the blade–vortex interaction phenomenon. The rotor was trimmed toward the experimental hub loads using a weak coupling strategy between CFD and a flight mechanics code.

It was shown that the tip vortex can be captured by a vortex-adapted grid that is prescribed using an analytical approach for the tip vortex trajectory. A special treatment for the Chimera exchange became necessary to ensure the accurate flow transfer between the different grids with an acceptable performance.

The weak coupling strategy turned out to be well suited to obtain a trimmed solution and thus to allow for a meaningful comparison with the experimental data. However, for a torsionally soft rotor such as the Bo105 model rotor, the correct prediction of the pitching moment by the CFD method emerged to be the crucial point for the correct reproduction of the blade dynamics. In the present case, tip torsion and tip flapping distribution versus azimuth were reasonably well-predicted, but differences were observed for the mean values.

The potential of vortex-adapted grids was evaluated by the comparison of the sectional normal force distribution to the standard grid setup and to grid setups featuring refined background grids. For a given overall number of grid points, the application of vortex-adapted grids allows for an improvement in the prediction of BVI loads. However, for a second-order method in space, a grid spacing of 0.1 chord turned out to be greatly insufficient to provide the vortex conservation required for the correct prediction of the BVI airloads. The reproduction of the BVI loading was first made possible by the reduction of the vortex-grid cross-sectional spacing to 2% chord and a further refinement of the blade grids. Using this grid setup, a very good BVI airloads prediction was achieved for the retreating blade side. BVI is now also observed on the advancing blade side, but the amplitudes are still underestimated.

One future activity is to repeat the grid refinement study using RANS equations. However, we do not expect significant changes compared with the inviscid modeling. Furthermore, the influence of the trailing-edge tab should be evaluated more in detail to find the reason for the deviation of the torsional mean value. An improvement in the prediction of the elastic torsion will probably lead to an improvement in the $C_nMa^2$ prediction, especially on the advancing blade side. Currently, we extend our grid system to include the generic fuselage of the experimental test setup. Thus, we will be able to judge its influence on the blade dynamics and the rotor wake. Our final goal is to compute the noise signature of CFD to a computational aeroacoustics (CAA) method. We hope that the vortex conservation based on the application of vortex-adapted grids will allow for the reproduction of BVI noise.

## Acknowledgments

The authors would like to thank the HART consortium [DLR, German Aerospace Research Center; ONERA; NASA Langley; German-Dutch Wind Tunnels DNW; and the U.S. Army Aero-Flight Dynamics Directorate (AFDD)] for providing us with the HART-2 experimental results. Furthermore, the authors would like to thank the German Federal Ministry of Economics and Technology (BMWi) for its funding within the framework of the Complete Helicopter Advanced Computational Environment (CHANCE 2) project, grant 20H0303A.

## References


[1] Wagner, S., "On the Numerical Prediction of Rotor Wakes Using Linear and Non-Linear Methods," 38th Aerospace Sciences Meeting & Exhibit, Reno, NV, AIAA Paper 2000-0111, Jan. 2000.

[2] Egolf, T. A., Wake, B. E., and Berezin, C., "Recent Rotor Wake Simulation and Modeling Studies at United Technologies Corporation," 38th Aerospace Sciences Meeting & Exhibit, Reno, NV, AIAA 2000-115, Jan. 2000.

[3] Röttgermann, A., Behr, R., Schöttl, C., and Wagner, S., "Calculation of Blade–Vortex Interaction of Rotary Wings in Incompressible Flow by an Unsteady Vortex-Lattice Method Including Free Wake Analysis," *Notes on Numerical Fluid Mechanics*, edited by W. Hackebusch, Numerical Techniques for Boundary Element Methods, Vol. 33, Vieweg, Brunswick, Germany, 1991, pp. 153–166.

[4] Berry, J. D., "A Multi-Element Vortex Lattice Method for Calculating the Geometry and Effects of a Helicopter Rotor Wake in Forward Flight," 26th Aerospace Sciences Meeting & Exhibit, Reno, NV, AIAA Paper 1988-0664, 1988.

[5] Krämer, E., Hertel, J., and Wagner, S., "Computation of Subsonic and Transonic Helicopter Rotor Flow Using Euler Equations," *Thirteenth European Rotorcraft Forum*, Association Aéronautique et Astronautique de France, Paris, 1987.

[6] Krämer, E., Hertel, J., and Wagner, S., "Euler Procedure for Calculation of the Steady Rotor Flow with Emphasis on Wake Evolution," *8th AIAA Applied Aerodynamics Conference*, AIAA, Reston, VA, 1990, pp. 132–142; also AIAA Paper 1990-3007.

[7] Chen, C. L., McCroskey, W. J., Obayashi, S., "Numerical Solutions of Forward Flight Rotor Flow Using an Upwind Method," *Journal of Aircraft*, Vol. 28, No. 6, 1991, pp. 374–380.

[8] Pahlke, K., "Extension of a 3-D Time-Accurate Euler Code to the Calculation of Multi-Bladed Rotors in Forward Flight Without Wake Modeling," *ECARP 2 (European Computational Aerodynamics Research Project 2): Validation of CFD Codes and Assessment of Turbulence Models*, Notes on Numerical Fluid Mechanics, Vol. 58, Vieweg, Brunswick, Germany, 1997, Chap. 2.11.

[9] Steger, J., Dougherty, N., and Benek, J., "A Chimera Grid Scheme," *Advances in Grid Generation*, edited by Ghia, K. N., and Ghia, U., Vol. 5, American Society of Mechanical Engineers, Fluid Engineering Div., New York, 1983, pp. 59–69.

[10] Meakin, R. L., "The Chimera Method of Simulation for Unsteady Three-Dimensional Viscous Flow," *Computational Fluid Dynamics Review*, edited by Hafez, M., and Oshima, K., Wiley, New York, 1995, pp. 70–86.

[11] Duque, E. P. N., and Srinivasan, G. R., "Numerical Simulation of a Hovering Rotor Using Embedded Grids," *AHS Annual Forum*, Vol. 48, American Helicopter Society, Alexandria, VA, 1992.

[12] Stangl, R., and Wagner, S., "Calculation of the Steady Rotor Flow Using an Overlapping Embedded Grid Technique," *Eighteenth European Rotorcraft Forum*, Association Aéronautique et Astronautique de France, Paris, 1992.

[13] Stangl, R., and Wagner, S., "Euler-Calculation of the Flow Field Around a Helicopter Rotor in Forward Flight," *Twentieth European Rotorcraft Forum*, Association Aéronautique et Astronautique de France, Paris, 1994.

[14] Stangl, R., and Wagner, S., "Euler Method to Calculate the Flow Around a Helicopter Using a Chimera Technique," *AHS Annual Forum*, Vol. 52, American Helicopter Society, Alexandria, VA, 1996.

[15] Boniface, J. C., and Pahlke, K., "Calculations of Multibladed Rotors in Forward Flight Using 3-D Euler Methods of DLR and ONERA," *22nd European Rotorcraft Forum 1996*, Royal Aeronautical Society, London, 1996.

[16] Yu, Y. H., Gmelin, B., Heller, H., Philippe, J. J., Mercker, E., and Preissler, J. S., "HHC Aeroacoustics Rotor Test at the DNW—The Joint German/French/US HART Project," *Twentieth European Rotorcraft Forum*, Association Aéronautique et Astronautique de France, Paris, 1994.

[17] Yu, Y. H., Tung, C., van der Wall, B., Pausder, H., Burley, C., Brooks, T., Beaumier, P., Delrieux, Y., Mercker, E., and Pengel, K., "The HART-2 Test: Rotor Wakes and Aeroacoustics with Higher-Harmonic Pitch Control (HHC) Inputs—The Joint German/French/Dutch/US Project," *AHS Annual Forum*, Vol. 58, American Helicopter Society, Alexandria, VA, 2002.

[18] Van der Wall, B., Junker, B., Burley, C., Brooks, T., Yu, Y. H., Tung, C., Raffel, M., Richard, H., Wagner, W., Mercker, E., Pengel, K., Holthusen, H., Beaumier, P., and Prieur, J., "The HART-2 Test in the LLF of the DNW—A Major Step Towards Rotor Wake Understanding," *28th European Rotorcraft Forum*, Royal Aeronautical Society, London, 2002.

[19] Servera, G., Beaumier, P., and Costes, M., "A Weak Coupling Method Between the Dynamics Code HOST and the 3-D Unsteady Euler Code WAVES," *26th European Rotorcraft Forum*, Royal Aeronautical Society, London, 2000.

[20] Altmikus, A., Wagner, S., Beaumier, P., and Servera, G., "A Comparison: Weak Versus Strong Modular Coupling for Trimmed Aeroelastic Rotor Simulations," *AHS Annual Forum*, Vol. 58, American Helicopter Society, Alexandria, VA, June 2002.

[21] Pahlke, K., and van der Wall, B., "Chimera Simulations of Multibladed Rotors in High-Speed Forward Flight with Weak Fluid-Structure Coupling," *Aerospace Science and Technology*, Vol. 9, No. 5, 2005, pp. 379–389.

[22] Dietz, M., Krämer, E., and Wagner, S., "Weak Coupling for Active Advanced Rotors," *31st European Rotorcraft Forum*, Royal Aeronautical Society, London, 2005.

[23] Benoit, B., Dequin, A.-M., Kampa, K., Grünhagen, W. v., Basset, P.-M., and Gimonet, B., "HOST: A General Helicopter Simulation Tool for Germany and France," *56th Annual Forum*, American Helicopter Society, Alexandria, VA, May 2000.

[24] Kroll, N., Eisfeld, B., and Bleecke, H. M., *The Navier–Stokes Code FLOWer*, Notes on Numerical Fluid Mechanics, Vol. 71, Vieweg, Brunswick, Germany, 1999, pp. 58–71.

[25] Schwarz, T., "The Overlapping Grid Technique for the Time-Accurate Simulation of Rotorcraft Flows," *31st European Rotorcraft Forum*, Royal Aeronautical Society, London, 2005.

[26] Hierholz, K.-H., and Wagner, S., "Simulation of Fluid-Structure Interaction at the Helicopter Rotor," *ICAS 98 Proceedings*, International Council of the Aeronautical Sciences, Stockholm, Sweden, and AIAA, Reston, VA, 1998.

[27] Hariharan, N. S., "A High Order Overset Refinement Methodology for Vortex-Dominated Flowfield Studies," 40th AIAA Aerospace Sciences Meeting & Exhibit, Reno, NV, AIAA Paper 2002-0965, 2002.

[28] Lee, Y., and Baeder, J. D., "Vortex Tracking Using Overset Grids for Quad Tilt Rotor in Forward Flight," 22nd Applied Aerodynamics Conference and Exhibit, Providence, RI, AIAA Paper 2004-5291, 2004.

[29] Egolf, T. A., and Landgrebe, A. J., "Helicopter Rotor Wake Geometry and Its Influence in Forward Flight," NASA CR-3726, 1983.

[30] Reichert, G., and Wagner, S., "Some Aspects of the Design of Rotor-Airfoil Shapes," *Aerodynamics of Rotary Wings*, AGARD CP-111, 1972.

[31] Lim, J. W., Tung, C., Yu, Y. H., Burley, C., Brooks, T., Boyd, D., van der Wall, B., Schneider, O., Richard, H., Raffel, M., Beaumier, P., Bailly, J., Delrieux, Y., Pengel, K., and Mercker, E., "HART-2: Prediction of Blade–Vortex Interaction Loading," *29th European Rotorcraft Forum*, Royal Aeronautical Society, London, 2003.

[32] Lim, J. W., Nygaard, T. A., Strawn, R., and Potsdam, M., "BVI Airloads Prediction Using CFD/CSD Loose Coupling," *Vertical Lift Aircraft Design Conference*, American Helicopter Society, Alexandria, VA, 2006.

[33] Jeong, J., and Hussain, F., "On the Identification of a Vortex," *Journal of Fluid Mechanics*, Vol. 285, 1995, pp. 69–94.


D. Gaitonde
*Associate Editor*